



Role of surface steps in activation of surface oxygen sites on Ir nanocrystals for oxygen evolution reaction in acidic media

Myeongjin Kim^a, Jinho Park^{b,c}, Maoyu Wang^d, Qingxiao Wang^e, Moon J. Kim^e, Jin Young Kim^f, Hyun-Seok Cho^g, Chang-Hee Kim^g, Zhenxing Feng^d, Byung-Hyun Kim^{h,*}, Seung Woo Lee^{b,*}

^a Department of Hydrogen & Renewable Energy, Kyungpook National University, 80 Daehakro, Bukgu, Daegu 41566, Republic of Korea

^b G. W. Woodruff School of Mechanical Engineering, Georgia Institute of Technology, Atlanta, GA 30332, USA

^c Aerospace, Transportation and Advanced Systems Laboratory, Georgia Tech Research Institute, Georgia Institute of Technology, Atlanta, GA 30332, USA

^d School of Chemical, Biological, and Environmental Engineering, Oregon State University, Corvallis, OR 97331, USA

^e Department of Materials Science and Engineering, University of Texas at Dallas, Richardson, TX 75080, USA

^f Center for Hydrogen-Fuel Cell Research, Korea Institute of Science and Technology (KIST), Hwarang-ro 14-gil 5, Seongbuk-gu, Seoul 02792, Republic of Korea

^g Hydrogen Research Department, Korea Institute of Energy Research, 152 Gajeong-ro, Yuseong-gu, Daejeon 34129, Republic of Korea

^h Platform Technology Laboratory, Korea Institute of Energy Research, 152 Gajeong-ro, Yuseong-gu, Daejeon 34129, Republic of Korea



ARTICLE INFO

Keywords:

Electrocatalysts

Oxygen evolution reaction

Operando X-ray absorption spectroscopy

Density functional theory

Ir nanocrystals

ABSTRACT

Ir and its oxide are the only available oxygen evolution reaction (OER) electrocatalysts with reasonably high activity and stability for commercial proton-exchange membrane electrolyzers. However, the establishment of structure–performance relationships for the design of better Ir-based electrocatalysts is hindered by their uncontrolled surface reconstruction during OER in acidic media. Herein, we monitor the structural evolution of two model Ir nanocrystals (one with a flat surface enclosed by (100) facets and the other with a concave surface containing numerous high-index planes) under acidic OER conditions. *Operando* X-ray absorption spectroscopy measurements reveal that the promotion of surface IrO_x formation during the OER by the concave Ir surface with high-index planes results in a gradual OER activity increase, while a decrease in activity and limited oxide formation are observed for the flat Ir surface. After the activation process, the Ir concave surface exhibits ~ 10 times higher activity than the flat surface. Density functional theory computations reveal that Ir high-index surfaces are thermodynamically preferred for the adsorption of oxygen atoms and the formation of surface oxides under OER conditions. Thus, our work establishes a structure–performance relationship for Ir nanocrystals under operating conditions, providing new principles for the design of nanoscale OER electrocatalysts.

1. Introduction

Electrochemical energy conversion and storage are the key enabling technologies for the efficient use of various renewable sources. In particular, solar-driven water splitting represents a state-of-the-art electrochemical technology that converts and stores energy in the form of hydrogen from intermittent renewable energies [1]. Proton-exchange membrane (PEM) electrolyzers operated under acidic conditions hold great promise for the sustainable production of hydrogen because of their high current densities, high-pressure operation, and fast hydrogen evolution reaction at the cathode [2]. However, the sluggish oxygen evolution reaction (OER) at the anode results in

significant overpotentials and energy losses during energy conversion [3–8], with the low stability of catalysts under the harsh acidic OER conditions presenting another critical challenge [9–11]. For example, most electrocatalysts that perform well in alkaline electrolytes are chemically unstable during acidic OER [12]. Currently, IrO_2 is the only available OER electrocatalyst with both reasonable activity and stability in acidic and oxidizing environments and is therefore widely used in commercial PEM electrolyzers [2,13]. Given that the high cost and scarcity of Ir limit the large-scale application of PEM electrolyzers [14], their efficiency and cost-effectiveness need to be increased via the development of more active and robust catalysts for acidic OER.

The cost-effectiveness of PEM electrolyzers can be increased by

* Corresponding authors.

E-mail addresses: bhkim@kier.re.kr (B.-H. Kim), seung.lee@me.gatech.edu (S.W. Lee).

improving the mass or specific OER activity of Ir-based catalysts. For instance, nanostructured Ir catalysts such as Ir-based nanocrystals [15, 16], nanodendrites [17], 3D superstructures [18], nanowires [19], Ir-skin frameworks [20], mesoporous nanosheets [21], cubic nanocages [22], nanoporous core-shell Ir/IrO₂ [23], and Ir single-atom catalysts [24–26] exhibit elevated OER activity primarily because of their increased surface area. In addition, various Ir mixed oxides such as perovskite-type SrIrO₃ [27–29], Ir-based double perovskites [30,31], and pyrochlore iridates (A₂Ir₂O₇, A = Pb, Bi, Y) [32,33] have been studied to increase acidic OER activity in correlation with their electronic and geometric structures. However, as these mixed oxides often undergo uncontrolled surface reconstruction during acidic OER [27,31, 34–36], the establishment of relationships between electronic/geometric structure and OER activity/stability is very challenging. Despite this difficulty, researchers have employed the surface reconstruction of metal oxides to design more active electrocatalysts for acidic OER, e.g., Jaramillo et al. showed that IrO_x/SrIrO₃ generated by surface rearrangement through the leaching of Sr from a perovskite SrIrO₃ thin film during acidic OER exhibits superior intrinsic activity [27]. Interestingly, the acidic OER activity of this thin film increased during electrochemical stability testing because of the *in situ* formation of IrO_x/SrIrO₃ [27]. A later study revealed that the gradual activity enhancement of IrO_x/SrIrO₃ during acidic OER is due to the Sr leaching-induced increase in electrochemical active area and the electronic structure modification caused by defect formation [37]. These results imply the importance of surface defects in Ir-based catalysts for determining OER activity under acidic conditions. Therefore, a deep understanding of structure–activity correlations under operating conditions is essential for the design of high-performance Ir-based OER catalysts.

Herein, we prepared two model Ir nanocrystals with flat and concave surfaces by controlled deposition of Ir overlayers on Pd nanocubes and monitored catalyst structure evolution under acidic OER conditions to elucidate the role of surface defects in promoting OER kinetics. A clear difference was observed in terms of OER activity and the formation of active IrO_x on the Ir surface. That is, the concave Ir surface with numerous high-index planes exhibited a progressive increase in OER activity due to the facile formation of surface IrO_x during the OER, while the flat Ir surface enclosed by (100) facets showed a gradual decrease in activity with restricted oxidation. After the OER activation process, concave-surface Ir nanocrystals exhibited a mass OER activity 10 times that of flat-surface nanocrystals and outperformed state-of-the-art Ir-based electrocatalysts. Density functional theory (DFT) computations revealed that Ir high-index surfaces such as Ir(553) are thermodynamically favorable for oxygen atom adsorption and oxide formation under OER conditions, thus explaining the high OER activity of the concave Ir surface. The results shed light on the structure–electrochemical performance relationships of surface structure–controlled Ir nanocrystals under acidic OER conditions and provide valuable insights for the design of new nanoscale catalysts for efficient PEM electrolyzers.

2. Experimental section

2.1. Materials

All chemicals were sourced from Sigma-Aldrich and used as received unless specified otherwise. These include Na₂PdCl₄ (98%), Na₃IrCl₆·xH₂O (< 100%), poly(vinylpyrrolidone) (PVP, M_w ≈ 55,000 Da), L-ascorbic acid (AA, 99%), KBr (99%), KCl (99%), ethylene glycol (EG, 99%, J. T. Baker), and ethanol (200 proof, KOPTEC). Aqueous solutions were prepared using deionized (DI) water with a resistivity of 18.2 MΩ cm.

2.2. Synthesis of Pd nanocubes

Pd nanocubes with edge lengths of 6 and 15 nm were synthesized as described elsewhere [38]. In the case of 15-nm Pd nanocubes, PVP (105

mg) and AA (60 mg) were dissolved in DI water (8 mL), and the solution was heated at 85 °C for 15 min upon magnetic stirring. After the rapid injection of an aqueous solution (3 mL) containing Na₂PdCl₄ (58 mg) and KBr (500 mg) into the preheated reaction solution, the mixture was further heated at 85 °C for 3 h upon magnetic stirring and then cooled to room temperature. In the case of 6-nm Pd nanocubes, a mixture of KBr (5 mg) and KCl (185 mg) was introduced instead of pure KBr (500 mg). The nanocubes were collected by centrifugation, washed with ethanol/DI water three times, and re-dispersed in EG (10 mL) for further use.

2.3. Synthesis of Pd@Ir flat and concave nanocubes

For the synthesis of Pd@Ir flat nanocubes (Pd@Ir f-nc), a suspension of 6-nm Pd nanocubes (4 mL), PVP (200 mg), AA (120 mg), and EG (20 mL) were mixed in a three-neck flask and heated at 100 °C for 1 h upon magnetic stirring. The temperature was then increased to 200 °C within 20 min, and an EG solution (12 mL) containing Na₃IrCl₆·xH₂O (6 mg) was dropwise added using a syringe pump at a rate of 4.0 mL h⁻¹. After the injection, the reaction mixture was maintained at 200 °C for 15 min upon magnetic stirring and then cooled to room temperature.

For the synthesis of Pd@Ir concave nanocubes (Pd@Ir c-nc), a suspension of 15-nm Pd nanocubes (1 mL), PVP (50 mg), AA (25 mg), KBr (100 mg), and EG (4 mL) were mixed in a three-neck flask, and the solution was heated at 200 °C for 1 h upon magnetic stirring. A solution of Na₃IrCl₆·xH₂O (2.28 mg), PVP (125 mg), and KBr (100 mg) in EG (10 mL) then dropwise added using a syringe pump at a rate of 0.5 mL h⁻¹. After the injection, the reaction mixture was maintained at 200 °C for 1 h upon magnetic stirring and then cooled to room temperature. The nanocubes were collected by centrifugation, washed three times with ethanol/DI water, and re-dispersed in ethanol.

2.4. Loading of Pd@Ir flat/concave nanocubes on carbon supports

A certain amount of Pd@Ir flat/concave nanocube suspension was dropwise injected via a pipette into an ethanolic suspension of carbon black (Vulcan XC-72, Cabot) to obtain a loading of ~ 20 wt% for both Ir and Pd. The mixture was then ultrasonicated for 3 h, and the resulting carbon-supported Pd@Ir nanocubes were collected by centrifugation, washed three times with ethanol/DI water, and oven-dried at 60 °C for 6 h prior to electrochemical tests.

2.5. Electrochemical measurements

Electrochemical measurements were performed using a glassy carbon rotating disk electrode (RDE, Pine Research Instrumentation) connected to a galvanic-/potentiostat (VMP3, BioLogic). Catalyst ink was prepared by adding carbon-supported Pd@Ir nanocubes (2 mg) to a mixture of DI water (1 mL), isopropanol (1 mL, Sigma-Aldrich), and Nafion (5 wt% solution, Sigma-Aldrich, 40 μL) followed by 10-min sonication. The working electrode was prepared by loading the ink (20 μL) onto a glassy carbon electrode. The Ir loading density of Pd@Ir f-nc and Pd@Ir c-nc catalysts on the RDEs were 8.2 and 5.4 μg_{Ir} cm⁻²_{RDE}, respectively. A reversible hydrogen electrode (RHE, Gaskatel) and a Pt rod were used as reference and counter electrodes, respectively, and 0.1 M aqueous HClO₄ (70%, double-distilled, GFS Chemicals) was used as the electrolyte. The residual impurities on the catalyst particle surface were removed by subjecting the electrode to a potential of -0.05 V vs. RHE for 1 min at room temperature. Cyclic voltammograms were recorded in an Ar-saturated electrolyte by cycling between 0.05 and 1.0 V vs. RHE at 0.05 V s⁻¹. Electrochemical surface area (ECSA) was determined from the charges generated from hydrogen adsorption and desorption between 0.08 and 0.4 V vs. RHE using a reference value of 210 μC cm⁻² for underpotentially deposited hydrogen from a Ir surface. OER polarization curves were recorded following the pre-oxidation of Ir, which was conducted by 25 potential sweep cycles in the range of 1.0–1.45 V vs. RHE. The OER test was carried out by sweeping the

potential in the range of 1.2–1.7 V vs. RHE in an Ar-saturated electrolyte at a scan rate of 0.01 V s⁻¹ and a rotation speed of 1600 rpm. All polarization curves were *iR*-corrected. The resistance (*R*) of the three-electrode system was measured to be 25–30 Ω, which was mainly due to the resistance of the liquid electrolyte (0.1 M HClO₄). In durability tests, OER polarization curves were recorded after 2, 4, 6, 8, and 10 h chronoamperometric measurements at 1.53 V vs. RHE.

2.6. Characterization

Transmission electron microscopy (TEM) imaging was performed using an HT7700 microscope (Hitachi) operated at 120 kV. High-angle annular dark-field scanning TEM and energy-dispersive X-ray (EDX) analyses were performed using an ARM200F microscope (JEOL) with a STEM aberration corrector operated at 200 kV. Metal contents were quantified by inductively coupled plasma-mass spectrometry (NexION 300Q, Perkin-Elmer). For the ICP-MS measurements, the catalysts were completely digested into aqua regia (HCl:HNO₃ = 3:1 by vol.) at 80 °C for 12 h and then diluted with 1% HNO₃ aqueous solution. X-ray photoelectron spectroscopy analysis was performed on a PHI 5000 VersaProbe II instrument (Japan) with a monochromatic Al K_α (*hν* = 1486.69 eV) X-ray source. X-ray absorption spectroscopy (XAS) measurements were performed at the BL7D beamline of the Pohang Light Source operating in the top-up mode at a ring current of 300 mA@3.0 GeV. The incident beam was collimated by a Ru-coated mirror at 2.8 mrad and monochromatized using a channel-cut Si (111) monochromator. The acquired extended X-ray absorption fine structure (EXAFS) data were processed according to standard procedures using the ATHENA module implemented in IFEFFIT software packages. EXAFS spectra were obtained by subtracting the post-edge background from the overall absorption followed by normalization with respect to the edge-jump step. Subsequently, the $\chi(k)$ data in *k*-space were Fourier-transformed to real (*R*) space using a Hanning window to separate the EXAFS contributions from different coordination shells. *Operando* XAS analysis was conducted in 0.1 M aqueous HClO₄ using an in-house-developed three-electrode configuration comprising an as-prepared electrocatalyst-based air electrode, the RHE, and a Pt rod as working, reference, and counter electrodes, respectively. Briefly, X-ray photons entered the air electrode through its backside, and fluorescent photons exiting the electrode were detected at 90° relative to the incident beam, which enabled the collection of catalyst XAS spectra during the electrochemical process. The electrocatalyst-based air electrode was fabricated using glassy carbon plates as working electrodes and substrates for catalysts. The as-prepared catalyst ink was dropped onto the plates and fully dried, and the resulting working electrode was attached to cells with a fast-curing epoxy resin (Devcon). Conductive Cu tape was attached to the backside of the working electrode to form an electrical connection. *Operando* XAS measurements were carried out in top-up mode at a ring current of 300 mA@3.0 GeV, and data were acquired at potentials between 1.47 and 1.53 V vs. RHE, with the applied potential stabilized for 5 min before XAS experiments. The coordination numbers extracted from the *operando* EXAFS Ir *L*₃-edge spectra were fixed as the normal values. The obtained S₀² was fixed as 0.7 during EXAFS fitting of *L*₃-edge spectra based on the known structure of Ir foil. For the simulation at the Ir *L*₃-edge data, the theoretical models used for the EXAFS fitting were generated from the Ir foil (Ir-Ir path) and IrO₂ structure (Ir-O path).

2.7. Computational methods

Spin-polarized plane-wave density functional theory (DFT) calculations were performed using the Vienna ab initio simulation package [39–42]. The projector-augmented wave method [43,44] was used for the explicit treatment of H 1s, O 2s & 2p, Ir 5d & 6s, Pd 4d & 5s electrons, while the core electrons were assumed to be frozen. The Perdew–Burke–Ernzerhof exchange-correlation functional within the

generalized gradient approximation was used [45]. The cut-off energy for the plane wave basis set was set to 500 eV. The convergence criterion for the total electronic energy was set to 10⁻⁶ eV. Geometry optimizations for all model structures were carried out until the maximal force acting on each atom was less than 0.02 eV Å⁻¹. The Brillouin zone was sampled using the Monkhorst-Pack scheme [46] with 2 × 2 × 1 *k*-points. For model structures, we considered Ir metal slabs with five different crystallographic orientations, namely (100), (110), (111), (311), and (553). Ir(311) and Ir(553) were chosen as representative surfaces for a concave surface (Fig. 3d). The exposed surface was decorated with atomic steps, as Pd@Ir c-nc should have atomic steps on its concave surfaces. Moreover, a stepped (553) surface is commonly observed for fcc metals such as Pt, Rh, and Pd [47–49]. Each slab model structure comprised five atomic layers. A vacuum region of 15 Å along the z-axis normal to the surface, which was sufficient to suppress the undesired image-image interactions, was introduced for all considered systems. All atoms within the top three layers were allowed to fully relax, while the bottom two layers were fixed to mimic a thick bulk layer. The atomic structures of suboxide layers for low-index surface orientations such as Ir (100), Ir(110), and Ir(111) were constructed as suggested elsewhere [50, 51], while the suboxide on Ir(311) and Ir(553) was obtained by forming O–Ir–O trilayer structures on the surface and fully relaxing them.

The single O adsorption energy was calculated as

$$\Delta E_{\text{O}^*} = E_{\text{O}^*} - (E_* + E_{\text{H}_2\text{O}} - E_{\text{H}_2}) \quad (\text{S1})$$

where the asterisk denotes a bare surface. Thus, E_* , E_{O^*} , $E_{\text{H}_2\text{O}}$, and E_{H_2} are the DFT-calculated total energies of a bare surface, an O-adsorbed surface, and the gas phases of H₂O and H₂, respectively. Free energy was defined as

$$G = E^{\text{DFT}} + \text{ZPE} - TS \quad (\text{S2})$$

Then, the Gibbs free energy of O adsorption was calculated as

$$\Delta G_{\text{O}^*} = \Delta E_{\text{O}^*} + \Delta E_{\text{ZPE}} - T\Delta S \quad (\text{S3})$$

where ΔE_{ZPE} is the difference in zero-point energy between the adsorbed O and the gas phases of H₂O and H₂, and $T\Delta S$ is the entropic contribution to free energy. The values of ΔE_{ZPE} and $T\Delta S$ for H₂O and H₂ were taken from thermodynamic tables for gas-phase molecules at 0.035 bar and 300 K. The zero-point energies and vibrational entropies for O-adsorbed Ir surfaces with different orientations were obtained by calculating the vibrational frequencies based on finite differences.

Surface free energy as a function of the applied potential was calculated as suggested elsewhere [50,52].

$$\gamma(U) = \gamma_{\text{bare}} + \frac{G_{n\text{O}^*} - [G_* + n(G_{\text{H}_2\text{O}} - G_{\text{H}_2})] - neU}{A} \quad (\text{S4})$$

where γ_{bare} is the surface free energy of a bare surface, n is the number of O adsorbates in the given system, U is the applied potential, e is the electron charge, and A is the surface area. Note that the electrode potential used in this work was based on the computational hydrogen electrode scheme proposed by Nørskov et al. [53]. All atomic structures used in this work are shown in Figs. S25–S29.

3. Results and discussion

3.1. Synthesis and characterization of Pd@Ir nanocubes

The synthesis of Pd@Ir core-shell flat and concave nanocubes is schematically illustrated in Fig. 1a and b. Flat and concave Pd@Ir cubes were prepared by Ir overlayer deposition on Pd nanocubes with edge lengths of 6 nm (Pd nc-6 nm) (Fig. S1a and b) and 15 nm (Pd nc-15 nm) (Fig. S1c and d), respectively. Pd nanocubes featured slightly truncated corner sites and a surface mainly enclosed by (100) facets. In the synthesis of Pd@Ir f-nc, IrCl₆³⁻ ions were dropwise injected into the

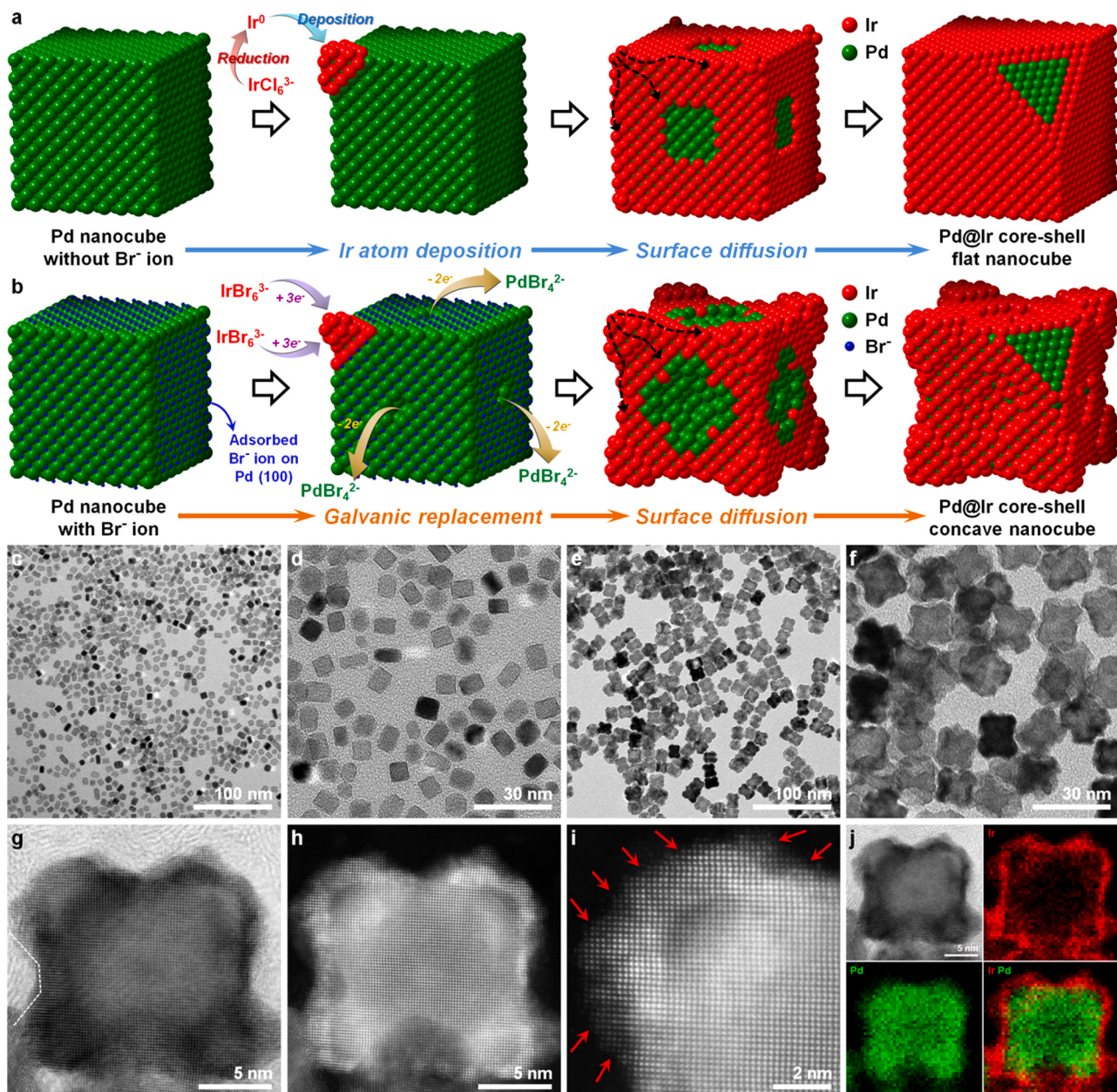


Fig. 1. Schematic synthesis of (a) Pd@Ir f-nc and (b) Pd@Ir c-nc. TEM images of (c, d) Pd@Ir f-nc and (e, f) Pd@Ir c-nc. (g) STEM image of Pd@Ir c-nc. (h, i) HAADF-STEM images of Pd@Ir c-nc. (j) STEM-EDX mappings of Ir and Pd in Pd@Ir c-nc.

reaction solution containing Pd nanocubes and were immediately reduced to Ir(0), which was preferentially deposited at nanocube corners and edges because of their higher (relative to that of flat (100) facets) surface energy [54,55]. Subsequently, the Ir adatoms diffused to the sides to produce Pd@Ir f-nc (Fig. 1a). In the synthesis of Pd@Ir c-nc, additional bromide ions were introduced into the reaction solution and were preferentially adsorbed onto the Pd(100) facets, effectively capping the side faces of Pd cubes. Bromide ions were also incorporated into the Ir precursor solution to convert IrCl₆³⁻ to IrBr₆³⁻. As IrBr₆³⁻ ions are thermodynamically more stable (i.e., have a higher reduction potential) than IrCl₆³⁻ ions, the former could not be immediately reduced to Ir(0) [56]. Once IrBr₆³⁻ ions had been deposited onto the corners and edges of the Pd nanocubes, they were reduced to Ir(0) by side facet Pd(0) atoms, which were converted into PdBr₄²⁻ ions that dissolved in the reaction solution [57]. Thus, in the early stage of precursor injection, such galvanic replacement caused Ir atoms to be selectively deposited at the corner/edge sites of Pd cubes while the side

faces were excavated to afford a concave surface. The Ir adatoms then slightly diffused from the corners/edges to the side faces of the cubes to produce Pd@Ir c-nc (Fig. 1b).

The flat and concave surface structures of Pd@Ir f-nc (Fig. 1c and d) and Pd@Ir c-nc (Fig. 1e and f) with uniform crystal shapes and sizes were characterized by TEM. In addition, the core-shell structure of Pd@Ir f-nc and the geometry of the undercoordinated Ir atoms in Pd@Ir c-nc were further probed by scanning transmission electron microscopy (STEM) coupled with EDX analysis. In the case of Pd@Ir c-nc, the side faces of Pd cubes were partially etched away during Ir deposition to form a concave shape (white dotted line in Fig. 1g), whereas the overall Pd cube shape was well preserved during the deposition of conformal Ir overlayers in the case of Pd@Ir f-nc (Figs. 1d and S2). In particular, many undercoordinated Ir atoms (red arrows in Fig. 1i) were observed on the surfaces of Pd@Ir c-nc by atomic-resolution high-angle annular dark-field (HAADF) STEM (Fig. 1h and i), and the concave core-shell structure of this nanocrystal was further confirmed by STEM-EDX

analysis (Fig. 1j). We recorded the XRD patterns of Pd@Ir c-nc and Pd@Ir f-nc (Fig. S3). The major peaks were observed between the reference peaks of Pd and Ir, indicating that Pd and Ir face-centered cubic structures coexist in both nanocrystals.

XPS and XAS analyses were employed to investigate the primary oxidation states of Ir and Pd in Pd@Ir f-nc and Pd@Ir c-nc. The Ir 4f_{7/2} (60.9 eV) and Ir 4f_{5/2} (63.9 eV) peaks and the Pd 3d_{5/2} (335.8 eV) and Pd 3d_{3/2} (341 eV) peaks indicated that both Pd@Ir f-nc and Pd@Ir c-nc comprised metallic Ir and Pd (Fig. S4). Furthermore, the absorption edges in X-ray absorption near-edge structure (XANES) spectra and the reduced distances of metallic Ir–Ir and Pd–Pd peaks in Fourier-transform extended EXAFS spectra of both catalysts were nearly identical to those of metallic Pd and Ir foils, confirming the metallic phase of Ir and Pd (Fig. S5).

3.2. Electrocatalytic performance of Pd@Ir nanocubes toward acidic OER

For OER performance evaluation, the Pd@Ir nanocubes were loaded onto a porous carbon support (Vulcan XC-72, Cabot; Figs. S6 and S7). Specific ECSAs were determined from the cyclic voltammetry (CV) curves of catalysts recorded in Ar-saturated 0.1 M HClO₄ at 0.05–1.0 V vs. reversible hydrogen electrode (RHE) (Fig. S8a). Based on the adsorption/desorption peaks of underpotentially deposited protons (H_{UPD}) in the potential range of 0.05–0.35 V vs. RHE, the ECSAs of Pd@Ir f-nc and Pd@Ir c-nc were calculated as 47.5 and 60.1 m² g⁻¹, respectively (Fig. S8b). Given that these nanocrystals were much larger than conventional Ir nanoparticles (Ir/C catalysts with a diameter of 2–3 nm and an ECSA of 59 m² g⁻¹ Ir) [58], the measured ECSAs were remarkably high, indicating that Ir atoms were well distributed on the Pd nanocubes as ultrathin overlayers. Prior to OER measurements, Ir in catalysts was pre-oxidized via repeated potential sweeping in the range of 1.0–1.45 V vs. RHE in Ar-saturated 0.1 M HClO₄ (Fig. S9), and OER activity was subsequently determined from linear sweep voltammetry (LSV) curves recorded at 1.2–1.7 V vs. RHE in Ar-saturated 0.1 M HClO₄

(Fig. S10). To confirm the potential contribution of Pd nanocubes to the OER, we conducted LSV measurements with the Pd nanocubes (Pd nc-6 nm and the Pd nc-15 nm) (Fig. S10). Both Pd nc-6 nm and Pd nc-15 nm showed significantly lower activity compared to Pd@Ir f-nc and Pd@Ir c-nc, confirming that the contribution of the Pd nanocubes to the OER activity was negligible.

The LSV curves and Tafel plots normalized by ECSA (Fig. 2a and inset) reveal that Pd@Ir c-nc exhibited significantly higher specific activity for acidic OER than Pd@Ir f-nc. Specifically, Pd@Ir c-nc showed current densities of 1.8 and 3.32 mA cm⁻² ECSA at 1.53 and 1.55 V vs. RHE, respectively, which were much higher than those of Pd@Ir f-nc (0.46 and 0.88 mA cm⁻² ECSA, respectively) (Fig. S11a). The higher specific activity of the former catalyst suggested the importance of high-index facets for acidic OER performance. Additionally, Pd@Ir c-nc delivered a 4–5 times higher mass activity (A g⁻¹ Ir) than Pd@Ir f-nc (Fig. S11b). It should be noted that both Pd@Ir f-nc and Pd@Ir c-nc exhibited significantly enhanced specific activity compared to an Ir/C catalyst (Fig. S12, 0.11 mA cm⁻² ECSA at 1.53 V and 0.24 mA cm⁻² ECSA at 1.55 V, Tafel slope = 89 mV dec⁻¹). To further confirm the effect of charge transfer on the catalytic reaction, electrochemical impedance spectroscopy (EIS) was recorded for both nanocrystals from 100 kHz to 0.1 Hz at 1.53 V (vs. RHE) with an amplitude of 10 mV (Fig. S13). Pd@Ir c-nc showed a lower R_{ct} (29.5 Ω) than Pd@Ir f-nc (39.4 Ω). This indicates that Pd@Ir c-nc has a higher charge transfer rate for OER, which is consistent with the lower Tafel slope compared to its counterpart (Fig. 2a).

Long-term catalyst stability was evaluated by 10 h chronoamperometric measurements at 1.53 V vs. RHE, with LSV curves recorded every 2 h (Fig. 2b and c). The current density of Pd@Ir f-nc slowly decreased over 10 h, but that of Pd@Ir c-nc showed negligible changes (Fig. 2b). Interestingly, the above LSV curves revealed that Pd@Ir c-nc showed a gradual increase in OER activity with time, whereas Pd@Ir f-nc exhibited the opposite behavior (Fig. 2c). Additionally, the Tafel slope of Pd@Ir c-nc decreased from 61 to 52 mV dec⁻¹ after the 10 h

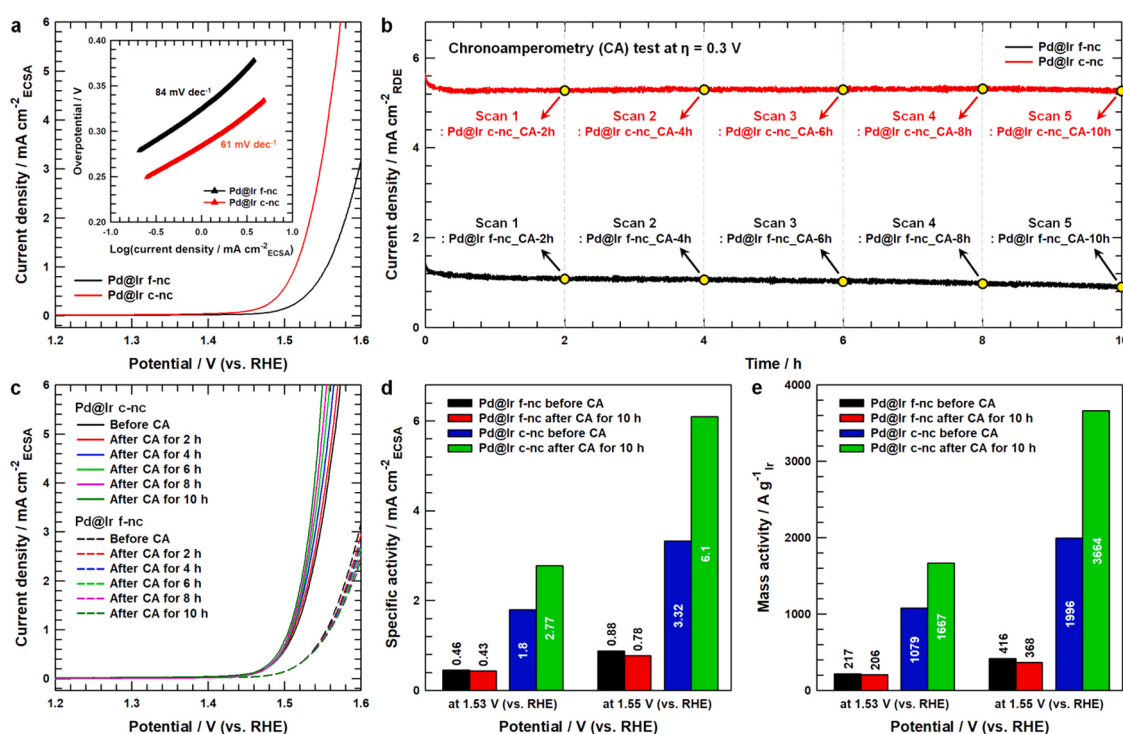


Fig. 2. (a) OER polarization curves and the corresponding Tafel plots (inset) of Pd@Ir f-nc and Pd@Ir c-nc recorded at 10 mV s⁻¹ and 1600 rpm in Ar-saturated 0.1 M HClO₄. Currents were normalized to ECSA obtained from H_{UPD} after iR-correction. (b) Chronoamperometry curves of Pd@Ir f-nc and Pd@Ir c-nc recorded at 1.53 V vs. RHE for 10 h. (c) OER polarization curves of Pd@Ir f-nc and Pd@Ir c-nc recorded during chronoamperometry test at 2 h intervals. (d) Specific and (e) mass activities of Pd@Ir f-nc and Pd@Ir c-nc at 1.53 and 1.55 V vs. RHE before/after 10 h chronoamperometric testing.

chronoamperometric measurement, whereas that of Pd@Ir f-nc increased from 84 to 91 mV dec⁻¹ (Fig. S14). As a result, Pd@Ir c-nc showed a significant increase in specific activity (from 3.3 to 6.1 mA cm⁻² ECSA) and mass activity (from 1996 to 3664 A g⁻¹ Ir) at 1.55 V vs. RHE after the 10 h chronoamperometry test, whereas both the specific and mass activities of Pd@Ir f-nc slightly decreased under these conditions (Fig. 2d and e). Accordingly, after the chronoamperometry test, the enhancement factor of Pd@Ir c-nc with respect to Pd@Ir f-nc at 1.55 V vs. RHE increased from 3.8 to 7.8 for specific activity and from 4.8 to 10 for mass activity. In addition, the high mass activity of Pd@Ir c-nc (3664 A g⁻¹ Ir) after activation exceeded those of state-of-the-art Ir-based electrocatalysts (Table S1).

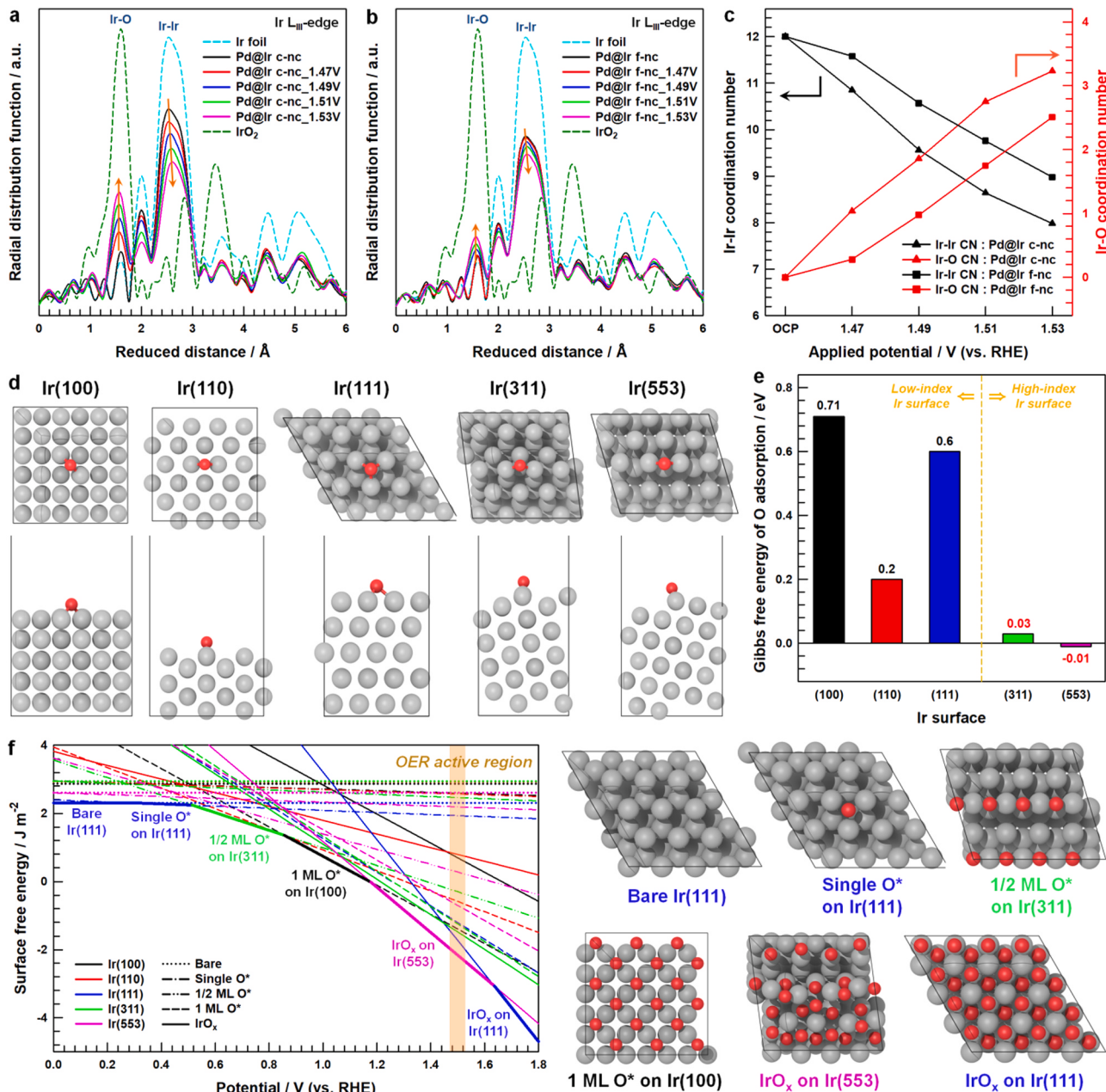


Fig. 3. *Operando* Ir L_{III}-edge EXAFS spectra of (a) Pd@Ir c-nc and (b) Pd@Ir f-nc recorded at 1.47–1.53 V vs. RHE in Ar-saturated 0.1 M HClO₄. (c) Ir-Ir and Ir-O CN changes extracted from L_{III}-edge EXAFS spectra as a function of applied potential. (d) Atomic configurations of single O-adsorbed Ir surfaces and (e) Gibbs free energies of O adsorption. (f) Surface free energy as a function of applied potential for Ir(100), Ir(110), Ir(111), Ir(311) and Ir(553) with O adsorption and IrO_x formation. Top view of atomic configurations for bare Ir(111), 1/16 mL O* (single O*) on Ir(111), 1/2 mL O* on Ir(311), 1 mL O* on Ir(100), IrO_x on Ir(553), and IrO_x on Ir(111). The Ir(553) surface comprises (111) terraces with a width of five atomic rows and a (111) faceted step separating the (111) terraces, which can be denoted as 5(111) × (111), while the Ir(311) surface is a stepped surface comprising (111) terraces with a width of two atomic rows and separated by a monoatomic (100)-type step, which can be denoted as 2(111) × (100).

3.3. Operando XAS analyses of Pd@Ir nanocubes during acidic OER

In addition, the progressive activation of Pd@Ir c-nc during the OER resembled that observed for $\text{IrO}_x/\text{SrIrO}_3$ [27], strongly suggesting the occurrence of surface rearrangement on the concave surface. The structural changes of the two model catalysts under acidic OER conditions were elucidated via *operando* XAS analysis. Fig. S16 shows the *operando* Pd K-edge XANES and EXAFS spectra of Pd@Ir f-nc and Pd@Ir c-nc recorded at various applied potentials, revealing that only negligible spectral changes were observed with increasing potential for both catalysts and thus indicating the absence of structural changes in Pd core nanocubes during the OER. On the other hand, the *operando* Ir L_{III}-edge XANES spectra of Pd@Ir c-nc showed a gradual positive shift, and the intensity of the white-line region increased with increasing applied potential (Fig. S17a). This behavior indicated the gradual formation of an IrO_x layer (the active phase for acidic OER [35]) and an increase in the average Ir oxidation state with increasing potential. However, the *operando* Ir L_{III}-edge XANES spectra of Pd@Ir f-nc showed that the degree of electrochemical oxidation from Ir to IrO_x was much lower than in the case of Pd@Ir c-nc (Fig. S17b). The calculation of the specific average Ir oxidation state relies on the availability of second-derivative XANES spectra. Edge position (the minimum of the second-derivative spectrum) was determined as a function of oxidation state for representative reference materials (Fig. S18a and b) to derive a first-order linear equation (Fig. S18c) that was used in combination with the edge positions derived from the second-derivative spectrum (Fig. S19) to establish the dependence of the average Ir oxidation states of Pd@Ir c-nc and Pd@Ir f-nc on applied potential (Fig. S20). Specifically, the average Ir oxidation state of Pd@Ir c-nc increased to 3.88 at an applied potential of 1.53 V vs. RHE, which is close to the valence state of the OER-active IrO_x species, whereas a trivial increase of the Ir oxidation state to 1.92 was observed for Pd@Ir f-nc.

The electrochemical oxidation of metallic Ir to IrO_x was further probed by EXAFS analysis. With increasing applied potential, the metallic Ir–Ir peak in the *operando* Ir L_{III}-edge EXAFS spectrum of Pd@Ir c-nc lost intensity, whereas the Ir–O peak gained intensity, which further confirmed the gradual formation of IrO_x (Fig. 3a). However, the extent of Ir–Ir and Ir–O peak intensity change for Pd@Ir f-nc was lower than that of Pd@Ir c-nc, indicating poor surface reconstruction from Ir to IrO_x (Fig. 3b). The degree of surface reconstruction was further investigated via the extraction of potential-dependent Ir–Ir and Ir–O coordination numbers (CNs) by fitting the *operando* Ir L_{III}-edge EXAFS spectra (Fig. S21 and Table S2). The conversion of Ir to IrO_x changed the Ir–Ir and Ir–O coordination environments, resulting in a decrease in Ir–Ir CN and an increase in Ir–O CN with increasing applied potential (Fig. 3c). Importantly, Pd@Ir c-nc showed a much lower Ir–Ir CN and a higher Ir–O CN than Pd@Ir f-nc at all applied potentials, which indicated that surface reconstruction from Ir to IrO_x was more favored by the concave surface structure. Furthermore, *ex situ* Ir 4f spectra recorded after LSV scanning from 1.2 to 1.53 V vs. RHE showed that Pd@Ir c-nc featured higher deconvoluted Ir^{3+} and Ir^{4+} peak areas than Pd@Ir f-nc (Fig. S22), in line with *operando* XAS results. Therefore, compared to the flat Ir surface, the concave surface was concluded to favor the electrochemical oxidation of Ir metal to the highly active IrO_x phase, which accounted for the higher OER activity of Pd@Ir c-nc.

3.4. DFT calculations of formation IrO_x on different Ir facets

The facile electrochemical transformation of metallic Ir to IrO_x for Pd@Ir c-nc can be attributed to the large number of undercoordinated Ir sites on the concave surface. We postulate that these sites were oxidized to higher-valence-state Ir in preference to fully coordinated Ir sites (Pd@Ir f-nc) because of the lower energy barrier for the formation of reactive oxygen atoms on the surface in the former case. Therefore, DFT calculations were performed to determine the origin of the facile oxidation activity of Pd@Ir c-nc in terms of atomic surface geometry.

The oxygen adsorption energy for various surface orientations of metallic Ir was calculated as a descriptor of the early stage of oxidation, as the oxidation process should start with the adsorption of oxygen on the surface. As a result, atomic oxygen preferred to occupy bridge sites for Ir(100) and Ir(110) and fcc hollow sites for Ir(111), while surface step sites were the preferred oxygen adsorption locations for both Ir(311) and Ir(553) (Fig. 3d and Table S3). The free energies of single O adsorption (ΔG_{O}^*) on high-index surfaces (0.03 eV for Ir(311) and –0.01 eV for Ir(553)) were significantly lower than those obtained for low-index surfaces (0.71 eV for Ir(100), 0.20 eV for Ir(110), and 0.60 eV for Ir(111)) (Fig. 3e). In addition, we performed additional DFT calculations to check if subsurface Pd atoms affect the oxygen adsorption on Ir surfaces since it was observed that the formed Ir shell is composed of a few atomic layers (Fig. 1j). The calculation results of oxygen adsorption on the Ir surfaces with subsurface Pd atoms show that the ΔG_{O}^* values on high-index surfaces with subsurface Pd atoms were also significantly lower than those obtained for low-index surfaces, which is in line with the cases of pure Ir metallic surfaces. (Figs. S23 and S24). Thus, these results indicated that Pd@Ir c-nc, which contained many more high-index planes, was more favorable for oxidation than Pd@Ir f-nc.

Next, we considered the thermodynamic stability of various Ir surfaces with different oxygen coverages and partially oxidized surfaces under electrochemical conditions to better understand the formation of IrO_x , which is known to be the active OER species. It should be noted that the actual oxidation is an electrochemical activation process involving not only Ir oxide formation via nucleation and growth, but also Ir hydroxide formation or Ir dissolution because of the instability of metallic Ir [59], which is beyond the scope of this study. Instead, a constrained ab initio thermodynamics approach for the evolution of Ir surface oxidation as a function of applied potential was adopted to investigate surface oxidation activity for different atomistic surface geometries in the electrochemical environment (Figs. 3f and S25–S29). Under ultrahigh vacuum conditions, the Ir(111) surface exhibited the lowest surface free energy of 2.30 J m^{-2} (cf. 2.87 J m^{-2} for Ir(100), 2.93 J m^{-2} for Ir(110), 2.94 J m^{-2} for Ir(311), and 2.61 J m^{-2} for Ir(553)). The single O-adsorbed Ir(111) surface became thermodynamically stable at an electrode potential of 0.31 V vs. RHE. In the potential range of 0.52–0.86 V vs. RHE, Ir(311) with a half monolayer (mL) coverage of oxygen was the most stable surface. The surface oxidation of Ir(100) started at 0.86 V vs. RHE as the 1 mL O-adsorbed Ir(100) surface became energetically stable. When the potential was further increased from 1.18 to 1.64 V vs. RHE, which is the OER range, the surface oxidation of Ir(553) afforded IrO_x . Interestingly, in this potential range (1.18–1.64 V vs. RHE), IrO_x was thermodynamically more stable on Ir(553) than on Ir(100). These results indicate that the facile surface oxidation of Pd@Ir c-nc stems from the large number of high-index surfaces that are thermodynamically more favorable for the adsorption of oxygen atoms and the formation of surface oxides under OER conditions.

The origin of the enhanced OER activity of Pd@Ir c-nc during long-term operation was further probed by *operando* XAS analysis during the 10 h chronoamperometry test at a constant applied potential of 1.53 V vs. RHE. This test was conducted when the potential of LSV scanning reached 1.53 V vs. RHE, and XANES and EXAFS spectra were recorded every 2 h. With increasing time, the Ir L_{III}-edge XANES spectra of Pd@Ir c-nc gradually shifted to higher energies, and the intensity of the white-line region also increased compared to that in the XANES spectrum recorded at 1.53 V vs. RHE (Fig. 4a). Conversely, the XANES spectra of Pd@Ir f-nc showed a slight positive shift and an intensity increase, with these minor changes saturating after 6 h of chronoamperometric testing (Fig. 4b). Based on the edge position derived from the second-derivative spectrum (Fig. 4c), the average Ir oxidation state of Pd@Ir c-nc gradually increased to 4.85 after 10 h chronoamperometric testing, while that of Pd@Ir f-nc slightly increased to 2.27 in 6 h and saturated until 10 h (Fig. S30). The different oxidation behaviors of the two catalysts were further revealed by *operando* Ir L_{III}-edge EXAFS analysis. When the

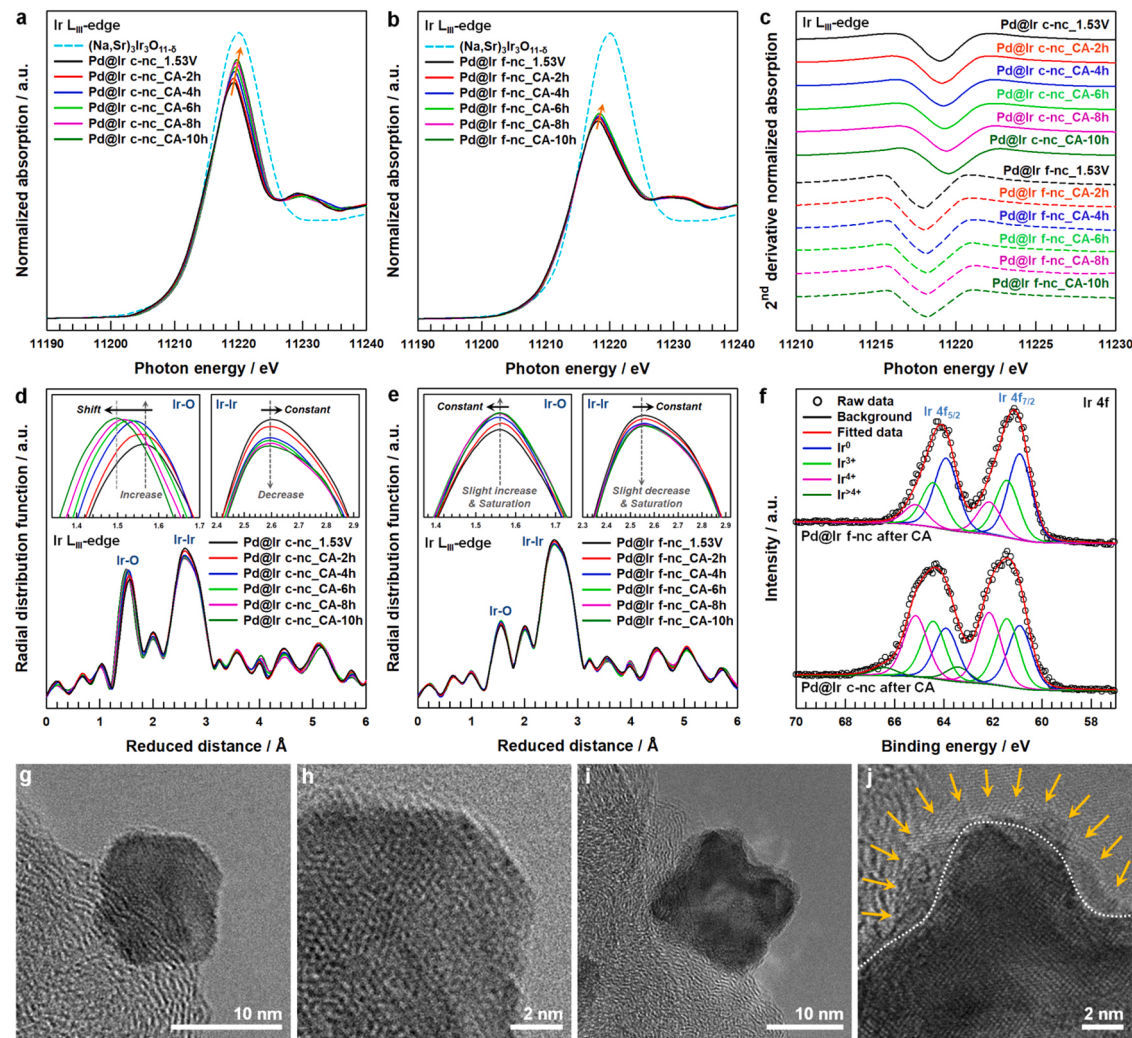


Fig. 4. *Operando* Ir L_{III}-edge XANES spectra of (a) Pd@Ir c-nc and (b) Pd@Ir f-nc recorded during the chronoamperometry test in Ar-saturated 0.1 M HClO₄ at 2 h intervals. (c) Corresponding *operando* second derivatives of Ir L_{III}-edge XANES absorption edge for Pd@Ir c-nc and Pd@Ir f-nc. *Operando* Ir L_{III}-edge EXAFS spectra of (d) Pd@Ir c-nc and (e) Pd@Ir f-nc recorded during the chronoamperometry test in Ar-saturated 0.1 M HClO₄ at 2 h intervals. (f) *Ex situ* Ir 4f spectra of Pd@Ir c-nc and Pd@Ir f-nc recorded after 10 h chronoamperometry test. HR-TEM images of (g, h) Pd@Ir f-nc and (i, j) Pd@Ir c-nc recorded after 10 h chronoamperometry test.

chronoamperometry test was performed for 4 h, the intensities of the Ir–Ir and Ir–O peaks gradually decreased and increased, respectively, indicating that an additional layer of IrO_x was formed on the Pd@Ir c-nc surface (Fig. 4d). After 4 h, the formation of the IrO_x layer was saturated, and the IrO_x species were further oxidized, as confirmed by the negative shift of the Ir–O reduced distance. The metal–oxygen bond distance in a metal oxide generally decreases with increasing oxidation state of the metal because of the concomitant reduction in the effective ionic radius [60]. However, for Pd@Ir f-nc, the intensities of metallic Ir–Ir and Ir–O bond peaks slightly decreased and increased during the 6 h chronoamperometry test, respectively, and finally saturated (Fig. 4e). In addition, the corresponding Ir–Ir and Ir–O CNs of Pd@Ir c-nc gradually decreased and increased, respectively, with the gradual formation of IrO_x during the chronoamperometry test, whereas in the case of Pd@Ir f-nc, these CNs saturated after 6 h (Figs. S31, S32 and Table S4). The results indicate that for Pd@Ir f-nc, the further oxidation of Ir to the OER-active IrO_x was difficult, in line with the low valence state of Ir (2.27). The *ex situ* Ir 4f spectrum of Pd@Ir c-nc also showed the emergence of the Ir^{>4+} peak after the chronoamperometry test (Fig. 4f), further supporting XAS results. Finally, the degree of IrO_x formation on flat and concave surfaces after 10 h chronoamperometry tests was investigated by high-resolution TEM (HR-TEM). It was difficult to detect the formation of an oxide layer on Pd@Ir f-nc (Fig. 4g and h), whereas

Pd@Ir c-nc (Fig. 4i and j) showed an apparent amorphous surface (orange arrows in Fig. 4j) with a high oxygen content (Fig. S33), which confirmed the formation of IrO_x under OER conditions. Overall, the key factor responsible for the activation of these Ir surfaces was identified as their ability to be oxidized under OER operating conditions.

4. Conclusions

In summary, model Ir nanocrystals with flat and concave surfaces were designed by carefully controlling the adsorption of Ir overlayers on Pd nanocubes. The Ir concave surface with high-index planes exhibited progressive activation for acidic OER catalysis, whereas the Ir flat surface enclosed by (100) facets showed a gradual decrease in activity. As a result, the activated Ir concave surface showed excellent OER activity that was 10 times higher than that of the flat surface and superior to those of most state-of-the-art Ir-based electrocatalysts. *Operando* XAS analyses revealed that this superior OER activity originated from the facile (compared to that on the flat surface) formation of active IrO_x. DFT calculations showed that high-index Ir surfaces are thermodynamically more favorable for the adsorption of oxygen atoms and the formation of IrO_x in the potential region of oxygen evolution, explaining the superior OER activity of the concave Ir surface. Furthermore, the *in situ* activation of the concave surface under acidic OER conditions was

associated with the progressive formation of IrO_x on high-index surfaces. The established structure–electrochemical performance relationship of the Ir nanocrystal system for acidic OER provides important insights for the design of highly active nanoscale electrocatalysts through their surface oxidation.

CRediT authorship contribution statement

Myeongjin Kim: Writing – original draft, Methodology, Conceptualization, Formal analysis, Investigation. **Jinho Park:** Writing – original draft, Methodology, Conceptualization, Formal analysis, Investigation. **Maoyu Wang:** Formal analysis, Investigation. **Qingxiao Wang:** Formal analysis, Investigation. **Moon J. Kim:** Formal analysis, Funding acquisition, Validation. **Jin Young Kim:** Funding acquisition, Validation. **Hyun-Seok Cho:** Funding acquisition, Validation. **Chang-Hee Kim:** Funding acquisition, Validation. **Zhenxing Feng:** Formal analysis, Investigation, Funding acquisition, Validation. **Byung-Hyun Kim:** Writing – original draft, Software, Methodology, Conceptualization, Investigation, Funding acquisition, Validation. **Seung Woo Lee:** Supervision, Writing – review & editing, Conceptualization, Funding acquisition, Validation, Project administration.

Declaration of Competing Interest

The authors declare that they have no known competing financial interests or personal relationships that could have appeared to influence the work reported in this paper.

Acknowledgments

M.K. and J.P. contributed equally to this work. This work was supported by the Korea Institute of Energy Technology Evaluation and Planning (KETEP) grant funded by the Korea government (MOTIE) (No. 20188550000440). This research was also supported by the Hydrogen Energy Innovation Technology Development Program of the National Research Foundation (NRF) of Korea funded by the Ministry of Science and ICT, South Korea (NRF-2019M3E6A1064020). This work was also supported by the National Research Foundation of Korea (NRF) grant funded by the Korea government (MSIT) (NRF-2021R1A4A1031761). M. J. Kim was supported in part by the Louis Beecherl Jr. Endowment Funds.

Appendix A. Supplementary material

Supplementary data associated with this article can be found in the online version at [doi:10.1016/j.apcatb.2021.120834](https://doi.org/10.1016/j.apcatb.2021.120834).

References

- [1] N.S. Lewis, D.G. Nocera, Powering the planet: chemical challenges in solar energy utilization, *Proc. Natl. Acad. Sci. USA* 103 (2006) 15729–15735.
- [2] M. Carmo, D.L. Fritz, J. Mergel, D. Stoltzen, A comprehensive review on PEM water electrolysis, *Int. J. Hydron. Energy* 38 (2013) 4901–4934.
- [3] M. Kim, J. Park, M. Kang, J.Y. Kim, S.W. Lee, Toward efficient electrocatalytic oxygen evolution: emerging opportunities with metallic pyrochlore oxides for electrocatalysts and conductive supports, *ACS Cent. Sci.* 6 (2020) 880–891.
- [4] W. Sheng, S.W. Lee, E.J. Crumlin, S. Chen, Y. Shao-Horn, Synthesis, activity and durability of Pt nanoparticles supported on multi-walled carbon nanotubes for oxygen reduction, *J. Electrochem. Soc.* 158 (2011) B1398–B1404.
- [5] M. Kim, J. Park, H. Ju, J.Y. Kim, H.-S. Cho, C.-H. Kim, B.-H. Kim, S.W. Lee, Understanding synergistic metal–oxide interactions of *in situ* exsolved metal nanoparticles on a pyrochlore oxide support for enhanced water splitting, *Energy Environ. Sci.* 14 (2021) 3053–3063.
- [6] L. Li, P. Wang, Q. Shao, X. Huang, Recent progress in advanced electrocatalyst design for acidic oxygen evolution reaction, *Adv. Mater.* (2021), 2004243.
- [7] L. An, C. Wei, M. Lu, H. Liu, Y. Chen, G.G. Scherer, A.C. Fisher, P. Xi, Z.J. Xu, C.-H. Yan, Recent development of oxygen evolution electrocatalysts in acidic environment, *Adv. Mater.* 33 (2021), 2006328.
- [8] T. Reier, H.N. Nong, D. Teschner, R. Schlögl, P. Strasser, Electrocatalytic oxygen evolution reaction in acidic environments – reaction mechanisms and catalysts, *Adv. Energy Mater.* 7 (2017), 1601275.
- [9] S. Cherevko, S. Geiger, O. Kasian, N. Kulyk, J.-P. Grote, A. Savan, B.R. Shrestha, S. Merzlikin, B. Breitbach, A. Ludwig, K.J.J. Mayrhofer, Oxygen and hydrogen evolution reactions on Ru, RuO_2 , Ir, and IrO_2 thin film electrodes in acidic and alkaline electrolytes: a comparative study on activity and stability, *Catal. Today* 262 (2016) 170–180.
- [10] R. Frydendal, E.A. Paoli, I. Chorkendorff, J. Rossmeisl, I.E.L. Stephens, Toward an active and stable catalyst for oxygen evolution in acidic media: Ti-stabilized MnO_2 , *Adv. Energy Mater.* 5 (2015), 1500991.
- [11] H. Jin, B. Ruiqia, Y. Park, H.J. Kim, H.-S. Oh, S.-I. Choi, K. Lee, Nanocatalyst design for long-term operation of proton/anion exchange membrane water electrolysis, *Adv. Energy Mater.* 11 (2021), 2003188.
- [12] S. Cherevko, A.R. Zeradjanin, A.A. Topalov, N. Kulyk, I. Katsounaros, K.J. Mayrhofer, Dissolution of noble metals during oxygen evolution in acidic media, *ChemCatChem* 6 (2014) 2219–2223.
- [13] H. Chen, L. Shi, X. Liang, L. Wang, T. Asefa, X. Zou, Optimization of active sites via crystal phase, composition, and morphology for efficient low-iridium oxygen evolution catalysts, *Angew. Chem. Int. Ed.* 59 (2020) 19654–19658.
- [14] P.C.K. Vesborg, T.F. Jaramillo, Addressing the terawatt challenge: scalability in the supply of chemical elements for renewable energy, *RSC Adv.* 2 (2012) 7933–7947.
- [15] J. Xu, Z. Lian, B. Wei, Y. Li, O. Bondarchuk, N. Zhang, Z. Yu, A. Araujo, I. Amorim, Z. Wang, B. Li, L. Liu, Strong electronic coupling between ultrafine iridium–ruthenium nanoclusters and conductive, acid-stable tellurium nanoparticle support for efficient and durable oxygen evolution in acidic and neutral media, *ACS Catal.* 10 (2020) 3571–3579.
- [16] N. Liu, Z. Duan, Q. Zhang, J. Guan, Insights into active species of ultrafine iridium oxide nanoparticle electrocatalysts in hydrogen/oxygen evolution reactions, *Chem. Eng. J.* 419 (2021), 129567.
- [17] H.-S. Oh, H.N. Nong, T. Reier, M. Gliech, P. Strasser, Oxide-supported Ir nanodendrites with high activity and durability for the oxygen evolution reaction in acid PEM water electrolyzers, *Chem. Sci.* 6 (2015) 3321–3328.
- [18] Y. Pi, N. Zhang, S. Guo, J. Guo, X. Huang, Ultrathin laminar Ir superstructure as highly efficient oxygen evolution electrocatalyst in broad pH range, *Nano Lett.* 16 (2016) 4424–4430.
- [19] L. Fu, F. Yang, G. Cheng, W. Luo, Ultrathin Ir nanowires as high-performance electrocatalysts for efficient water splitting in acidic media, *Nanoscale* 10 (2018) 1892–1897.
- [20] Y. Pi, Q. Shao, X. Zhu, X. Huang, Dynamic structure evolution of composition segregated iridium–nickel rhombic dodecahedra toward efficient oxygen evolution electrocatalysis, *ACS Nano* 12 (2018) 7371–7379.
- [21] B. Jiang, Y. Guo, J. Kim, A.E. Whitten, K. Wood, K. Kani, A.E. Rowan, J. Henzie, Y. Yamauchi, Mesoporous metallic iridium nanosheets, *J. Am. Chem. Soc.* 140 (2018) 12434–12441.
- [22] J. Zhu, Z. Chen, M. Xie, Z. Lyu, M. Chi, M. Mavrikakis, W. Jin, Y. Xia, Iridium-based cubic nanocages with 1.1-nm-thick walls: a highly efficient and durable electrocatalyst for water oxidation in an acidic medium, *Angew. Chem. Int. Ed.* 58 (2019) 7244–7248.
- [23] Y.-T. Kim, P.P. Lopes, S.-A. Park, A.Y. Lee, J. Lim, H. Lee, S. Back, Y. Jung, N. Danilovic, V. Stamenkovic, J. Erlebacher, J. Snyder, N.M. Markovic, Balancing activity, stability and conductivity of nanoporous core-shell iridium/iridium oxide oxygen evolution catalysts, *Nat. Commun.* 8 (2017) 1449.
- [24] J. Yin, J. Jin, M. Lu, B. Huang, H. Zhang, Y. Peng, P. Xi, C.-H. Yan, Iridium single atoms coupling with oxygen vacancies boosts oxygen evolution reaction in acid media, *J. Am. Chem. Soc.* 142 (2020) 18378–18386.
- [25] Q. Zhang, J. Guan, Applications of single-atom catalysts, *Nano Res.* (2021) 1–6, <https://doi.org/10.1007/s12274-021-3479-8>.
- [26] Q. Zhang, Z. Duan, Y. Wang, L. Li, B. Nan, J. Guan, Atomically dispersed iridium catalysts for multifunctional electrocatalysis, *J. Mater. Chem. A* 8 (2020) 19665–19673.
- [27] L.C. Seitz, C.F. Dickens, K. Nishio, Y. Hikita, J. Montoya, A. Doyle, C. Kirk, A. Vojvodic, H.Y. Hwang, J.K. Norskov, T.F. Jaramillo, A highly active and stable $\text{IrO}_x/\text{SrIrO}_3$ catalyst for the oxygen evolution reaction, *Science* 353 (2016) 1011–1014.
- [28] L. Yang, G. Yu, X. Ai, W. Yan, H. Duan, W. Chen, X. Li, T. Wang, C. Zhang, X. Huang, J.-S. Chen, X. Zou, Efficient oxygen evolution electrocatalysis in acid by a perovskite with face-sharing IrO_6 octahedral dimers, *Nat. Commun.* 9 (2018) 5236.
- [29] X. Liang, L. Shi, R. Cao, G. Wan, W. Yan, H. Chen, Y. Liu, X. Zou, Perovskite-type solid solution nano-electrocatalysts enable simultaneously enhanced activity and stability for oxygen evolution, *Adv. Mater.* 32 (2020), 2001430.
- [30] O. Diaz-Morales, S. Raaijman, R. Kortlever, P.J. Kooyman, T. Wezendonk, J. Gascon, W.T. Fu, M.T.M. Koper, Iridium-based double perovskites for efficient water oxidation in acid media, *Nat. Commun.* 7 (2016) 12363.
- [31] A. Grimaud, A. Demortière, M. Saubanère, W. Dachraoui, M. Duchamp, M.-L. Doublet, J.-M. Tarascon, Activation of surface oxygen sites on an iridium-based model catalyst for the oxygen evolution reaction, *Nat. Energy* 2 (2016) 16189.
- [32] W. Sun, J.-Y. Liu, X.-Q. Gong, W.-Q. Zaman, L.-M. Cao, J. Yang, OER activity manipulated by IrO_6 coordination geometry: an insight from pyrochlore iridates, *Sci. Rep.* 6 (2016) 38429.
- [33] P.-C. Shih, J. Kim, C.-J. Sun, H. Yang, Single-phase pyrochlore $\text{Y}_2\text{Ir}_2\text{O}_7$ electrocatalyst on the activity of oxygen evolution reaction, *ACS Appl. Mater. Interfaces* 1 (2018) 3992–3998.
- [34] C.W. Song, H. Suh, J. Bak, H.B. Bae, S.-Y. Chung, Dissolution-induced surface roughening and oxygen evolution electrocatalysis of alkaline-earth iridates in acid, *Chem. Mater.* 3 (2019) 3243–3259.
- [35] R. Zhang, N. Dubouis, M. Ben Osman, W. Yin, M.T. Sougrati, D.A.D. Corte, D. Giaume, A. Grimaud, A dissolution/precipitation equilibrium on the surface of

- iridium-based perovskites controls their activity as oxygen evolution reaction catalysts in acidic media, *Angew. Chem. Int. Ed.* 58 (2019) 4571–4575.
- [36] C.W. Song, J. Lim, H.B. Bae, S.-Y. Chung, Discovery of crystal structure–stability correlation in iridates for oxygen evolution electrocatalysis in acid, *Energy Environ. Sci.* 13 (2020) 4178–4188.
- [37] K. Lee, M. Osada, H.Y. Hwang, Y. Hikita, Oxygen evolution reaction activity in IrO_x/SrIrO₃ catalysts: correlations between structural parameters and the catalytic activity, *J. Phys. Chem. Lett.* 10 (2019) 1516–1522.
- [38] B. Lim, H. Kobayashi, P.H.C. Camargo, L.F. Allard, J. Liu, Y. Xia, New insights into the growth mechanism and surface structure of palladium nanocrystals, *Nano Res.* 3 (2010) 180–188.
- [39] G. Kresse, J. Hafner, The performance of a family of density functional methods, *Phys. Rev. B* 47 (1993) 558–561.
- [40] G. Kresse, J. Hafner, Ab initio molecular-dynamics simulation of the liquid-metal-amorphous-semiconductor transition in germanium, *Phys. Rev. B* 49 (1994) 14251–14269.
- [41] G. Kresse, J. Furthmüller, Efficient iterative schemes for ab initio total-energy calculations using a plane-wave basis set, *Phys. Rev. B* 54 (1996) 11169–11186.
- [42] G. Kresse, J. Furthmüller, Efficiency of ab-initio total energy calculations for metals and semiconductors using a plane-wave basis set, *Comput. Mater. Sci.* 6 (1996) 15–50.
- [43] P.E. Blöchl, Projector augmented-wave method, *Phys. Rev. B* 50 (1994) 17953–17979.
- [44] G. Kresse, D. Joubert, From ultrasoft pseudopotentials to the projector augmented-wave method, *Phys. Rev. B* 59 (1999) 1758–1775.
- [45] J.P. Perdew, K. Burke, M. Ernzerhof, Generalized gradient approximation made simple, *Phys. Rev. Lett.* 77 (1996) 3865–3868.
- [46] H.J. Monkhorst, J.D. Pack, Special points for Brillouin-zone integrations, *Phys. Rev. B* 13 (1976) 5188–5192.
- [47] I.T. McCrum, M.T.M. Koper, The role of adsorbed hydroxide in hydrogen evolution reaction kinetics on modified platinum, *Nat. Energy* 5 (2020) 891–899.
- [48] A. Stroppa, F. Mittendorfer, J.N. Andersen, G. Parteder, F. Allegretti, S. Suriev, F. P. Netzer, Adsorption and dissociation of CO on bare and Ni-decorated stepped Rh (553) surfaces, *J. Phys. Chem. C* 113 (2009) 942–949.
- [49] R. Westerström, J. Gustafson, A. Resta, A. Mikkelsen, J.N. Andersen, E. Lundgren, N. Seriani, F. Mittendorfer, M. Schmid, J. Klikovits, P. Varga, M.D. Ackermann, J. W.M. Frenken, N. Kasper, A. Stierle, Oxidation of Pd(553): from ultrahigh vacuum to atmospheric pressure, *Phys. Rev. B* 76 (2007), 155410.
- [50] K. Klyukin, A. Zagalskaya, V. Alexandrov, Ab initio thermodynamics of iridium surface oxidation and oxygen evolution reaction, *J. Phys. Chem. C* 122 (2018) 29350–29358.
- [51] Y.B. He, A. Stierle, W.X. Li, A. Farkas, N. Kasper, H. Over, Oxidation of Ir(111): from O–Ir–O trilayer to bulk oxide formation, *J. Phys. Chem. C* 112 (2008) 11946–11953.
- [52] I.T. McCrum, M.J. Janik, pH and alkali cation effects on the Pt cyclic voltammogram explained using density functional theory, *J. Phys. Chem. C* 120 (2016) 457–471.
- [53] J.K. Nørskov, J. Rossmeisl, A. Logadottir, L. Lindqvist, J.R. Kitchin, T. Bligaard, H. Jónsson, Origin of the overpotential for oxygen reduction at a fuel-cell cathode, *J. Phys. Chem. B* 108 (2004) 17886–17892.
- [54] S. Xie, S.-I. Choi, N. Lu, L.T. Roling, J.A. Herron, L. Zhang, J. Park, J. Wang, M. J. Kim, Z. Xie, M. Mavrikakis, Y. Xia, Atomic layer-by-layer deposition of Pt on Pd nanocubes for catalysts with enhanced activity and durability toward oxygen reduction, *Nano Lett.* 14 (2014) 3570–3576.
- [55] X. Xia, S. Xie, M. Liu, H.-C. Peng, N. Lu, J. Wang, M.J. Kim, Y. Xia, On the role of surface diffusion in determining the shape or morphology of noble-metal nanocrystals, *Proc. Natl. Acad. Sci. USA* 110 (2013) 201222109–2012226673.
- [56] D.C. Harris, Quantitative Chemical Analysis, 8th ed., Macmillan, New York, 2010.
- [57] H. Zhang, M. Jin, J. Wang, W. Li, P.H.C. Camargo, M.J. Kim, D. Yang, Z. Xie, Y. Xia, Synthesis of Pd–Pt bimetallic nanocrystals with a concave structure through a bromide-induced galvanic replacement reaction, *J. Am. Chem. Soc.* 133 (2011) 6078–6089.
- [58] J. Durst, A. Siebel, C. Simon, F. Hasché, J. Herranz, H.A. Gasteiger, New insights into the electrochemical hydrogen oxidation and evolution reaction mechanism, *Energy Environ. Sci.* 7 (2014) 2255–2260.
- [59] H. Jang, T.T. Hieu, S.H. Kim, J. Lee, Reduction of iridium loading to the minimum level required for water oxidation electrocatalysis without sacrificing the electrochemical stability, *J. Phys. Chem. C* 123 (2019) 12928–12934.
- [60] H.N. Nong, T. Reier, H.-S. Oh, M. Gleich, P. Paciok, T.H.T. Vu, D. Teschner, M. Heggen, V. Petkov, R. Schlögl, T. Jones, P. Strasser, A unique oxygen ligand environment facilitates water oxidation in hole-doped IrNiO_x core–shell electrocatalysts, *Nat. Catal.* 1 (2018) 841–851.